Since January 2020 Elsevier has created a COVID-19 resource centre with free information in English and Mandarin on the novel coronavirus COVID-19. The COVID-19 resource centre is hosted on Elsevier Connect, the company's public news and information website.

Journal of Theoretical Biology 564 (2023) 111449

Contents lists available at ScienceDirect

Journal of Theoretical Biology

journal homepage: www.elsevier.com/locate/yjtbi

Multiple cohort study of hospitalized SARS-CoV-2 in-host infection dynamics: Parameter estimates, identifiability, sensitivity and the eclipse phase profile

Chapin S. Korosec [a,b,*], Matthew I. Betti [c], David W. Dick [a,b], Hsu Kiang Ooi [d], Iain R. Moyles [a,b], Lindi M. Wahl [e], Jane M. Heffernan [a,b,*]

[a] Modelling Infection and Immunity Lab, Mathematics and Statistics, York University, 4700 Keele St, Toronto, M3J 1P3, ON, Canada
[b] Centre for Disease Modelling, Mathematics and Statistics, York University, 4700 Keele St, Toronto, M3J 1P3, ON, Canada
[c] Department of Mathematics and Computer Science, Mount Allison University, 62 York St, Sackville, E4L 1E2, NB, Canada
[d] Digital Technologies Research Centre, National Research Council Canada, 222 College Street, Toronto, M5T 3J1, ON, Canada
[e] Mathematics, Western University, 1151 Richmond St, London, N6A 5B7, ON, Canada

ARTICLE INFO

Keywords:
SARS-coV-2
Viral load
Eclipse phase
In-host model
Reproduction number
TEIV model
Structural identifiability
Practical identifiability

ABSTRACT

Within-host SARS-CoV-2 modelling studies have been published throughout the COVID-19 pandemic. These studies contain highly variable numbers of individuals and capture varying timescales of pathogen dynamics; some studies capture the time of disease onset, the peak viral load and subsequent heterogeneity in clearance dynamics across individuals, while others capture late-time post-peak dynamics. In this study, we curate multiple previously published SARS-CoV-2 viral load data sets, fit these data with a consistent modelling approach, and estimate the variability of in-host parameters including the basic reproduction number, R_0, as well as the best-fit eclipse phase profile. We find that fitted dynamics can be highly variable across data sets, and highly variable within data sets, particularly when key components of the dynamic trajectories (e.g. peak viral load) are not represented in the data. Further, we investigated the role of the eclipse phase time distribution in fitting SARS-CoV-2 viral load data. By varying the shape parameter of an Erlang distribution, we demonstrate that models with either no eclipse phase, or with an exponentially-distributed eclipse phase, offer significantly worse fits to these data, whereas models with less dispersion around the mean eclipse time (shape parameter two or more) offered the best fits to the available data across all data sets used in this work. This manuscript was submitted as part of a theme issue on "Modelling COVID-19 and Preparedness for Future Pandemics".

1. Introduction

Since late 2019, the SARS-CoV-2 virus has significantly disrupted life globally (Pokhrel and Chhetri, 2021; Xiong et al., 2020; Burki, 2020). Two years later, many countries are moving to consider SARS-CoV-2 and the resulting COVID-19 infection to be endemic (Liew and Robinson, 2022), which will require new strategies for forecasting, management and control. An endemic state will necessitate a sustained reliance on data fitting (Liew and Robinson, 2022), and on analytical tools, as public health authorities manage risk and allocate resources in future years.

Mathematical modelling has been employed in the estimation of key parameters of the evolution of SARS-CoV-2 outbreaks at the population level. Important predicted parameters have included the time dependent epidemiological reproduction number (Betti and Heffernan, 2021), the effects of quarantine and risk of importation (Arino et al., 2020; Moyles et al., 2021), the effects of aggregate non-pharmaceutical intervention (Betti and Heffernan, 2021), the risks associated with relaxing interventions competing with increasing vaccination (Betti et al., 2021b), and the effects of vaccination waning and boosting on case loads (Childs et al., 2021). All of these estimates can then be used with mathematical models that estimate the impact of COVID-19 on healthcare systems (Betti et al., 2021a).

Mathematical modelling has also been used to model SARS-CoV-2 in-host infection dynamics. Mathematical models at the in-host level can estimate parameters and outcomes that may be difficult to measure at the population level. For example, SARS-CoV-2 in-host models have

* Corresponding authors.
E-mail addresses: chapinSkorosec@gmail.com (C.S. Korosec), matthew.betti@gmail.com (M.I. Betti), dwdick@yorku.ca (D.W. Dick), hsukiang.ooi@nrc-cnrc.gc.ca (H.K. Ooi), imoyles@yorku.ca (I.R. Moyles), lwahl@uwo.ca (L.M. Wahl), jmheffer@yorku.ca (J.M. Heffernan).

https://doi.org/10.1016/j.jtbi.2023.111449
Received 22 June 2022; Received in revised form 9 February 2023; Accepted 22 February 2023
Available online 7 March 2023

been used to model the immune response generated by vaccines, to predict which populations vaccines are likely to impact most (Korosec et al., 2022) as well as determine significant immunological timescales of the vaccines (Moyles et al., 2022), to estimate the efficacy of vaccines in individuals (Farhang-sardroodi et al., 2021), model T cell and cytokine dynamics (Gholami et al., 2023), and model T cell dynamics and cytokine secretion in mild, moderate and severe cases of COVID-19 (Lin et al., 2022). A major focus of SARS-CoV-2 in-host modelling has been understanding viral load dynamics: examples include correlating viral load with mortality (Néant et al., 2021); linking viral load dynamics with host transmission (Goyal et al., 2021; Marc et al., 2021); understanding the effects of antiviral therapy on the shedding dynamics (Goyal et al., 2020); assessing individual-level heterogeneity in mild cases (Ke et al., 2022); and relating viral load with viral replication and the immune response (Challenger et al., 2022).

Recent studies have found that viral load levels in the upper respiratory track are similar in symptomatic and asymptomatic individuals (Ra et al., 2021), and further, that viral load can vary by five orders of magnitude and yet still display no correlation with disease severity (Challenger et al., 2022). In contrast, others have reported that high viral load titres are correlated with an increase in mortality as well as disease severity (Pujadas et al., 2020; Fajnzylber et al., 2020; Huang et al., 2020; Tsukagoshi et al., 2021; Westblade et al., 2020), suggesting that case severity (hospitalized versus non-hospitalized) may be an important factor in viral load. Furthermore, the time-to-peak, as well as magnitude of peak viral load, are informative in understanding the probability of transmission and when transmission is likely to occur throughout the course of the disease (Pan et al., 2020; Pujadas et al., 2020; Singanayagam et al., 2022). Correctly characterizing viral load dynamics with an accurate mathematical model is critical in accurately predicting disease outcomes and transmission dynamics.

It is important to note that SARS-CoV-2 in-host viral load studies can include cohorts of various sizes, in which individual shedding dynamics are collected at various points in time throughout the disease time-course and across the pandemic, both temporally and geographically. In addition, due to difficulties inherent in early data collection, many studies capture limited dynamics of the trajectory of viral load within a single individual. Using mathematical modelling and statistical fitting methods, in-host models and parameter estimation, relationships between different viral load data sets can be uncovered.

In the current study, we curated three previously published viral load data sets for which temporal viral load trajectories were available (Néant et al., 2021; Jones et al., 2021; Goyal et al., 2020), and fit each data set to a series of target-cell limited in-host models. The data sets used consist of primarily hospitalized individuals, and vary in size from 25 to 4344 individuals. Fitting these data sets to the same set of in-host models allows us to quantify the reliability and reproducibility of fitted parameter values, both within and among studies. We are also able to address how real-world constraints such as data sets containing fewer individuals, or data sets in which the peak response was not captured, affect the uncertainty of the fitted parameters and estimated reproduction number, R_0.

Previous SARS-CoV-2 in-host studies have employed an exponentially-distributed eclipse phase to describe viral load dynamics (Néant et al., 2021; Goyal et al., 2020; Gonçalves et al., 2020, 2021; Wang et al., 2020; Marc et al., 2021). The eclipse phase is included to model the delay between successful target cell infection and the production of virus; biologically, the input virion is "eclipsed" by the cell, initiating a multitude of processes that ends when the cell is able to productively bud new virions. The mean duration of this process, referred to as the mean eclipse time, varies between diseases, cell types, and most likely across various strains of the same virus. For example, the length of the eclipse phase for influenza virus has been found to vary between 6 to 12 h depending on the strain (Baccam et al., 2006a; Holder and Beauchemin, 2011; Pinilla et al., 2012; Simon et al., 2016). The probability distribution for duration of the eclipse phase takes into account the multiple timescales for the succession of biological mechanisms that end in viral budding, and also accounts for the stochastic variability inherent to these processes (Kakizoe et al., 2015). Incorporating a single eclipse compartment, as done in previous SARS-CoV-2 viral load studies (Néant et al., 2021; Goyal et al., 2020; Gonçalves et al., 2020, 2021; Wang et al., 2020; Marc et al., 2021), implicitly assumes an exponentially-distributed eclipse duration. Biologically, this corresponds to the unrealistic situation in which some cells will instantaneously enter a budding state at the moment of infection, neglecting eclipse dynamics entirely. The probability distribution for the eclipse phase duration for SHIV, for example, has been found to best be described by a fat-tailed distribution (Beauchemin et al., 2017), and for influenza by a normal or log-normal distribution (Holder and Beauchemin, 2011). Therefore, another focus of this work was to fit multiple published SARS-CoV-2 data sets to models with varying eclipse time distributions to assess via log-likelihood estimators (including penalties for additional parameters) if a particular model is preferred. We further explore how the probability distribution of the eclipse phase affects the reported R_0, both through considering many different fits to data with varying resolution, as well as analytically as the eclipse phase distributions are varied from exponential to Erlang, including comparing to no eclipse stage.

The main questions we address in this study are then two-fold: (1) by taking viral load data sets of varying resolution, how well can one estimate the standard parameters of the within-host model; in other words, to what extent do these parameters suffer from practical identifiability concerns previously not discussed in the literature, and (2) across all the data sets is there a preferred eclipse profile (as measured by AIC/BIC) whereby the eclipse stages are chained together through k exponentials with the mean eclipse time fixed to a literature-informed value. Thus, (2) seeks to answer whether or not an exponential or Erlang distribution is better suited to describe the eclipse profile.

2. Methods

2.1. Clinical data acquisition and summary

All viral load data sets used in this work were previously published, the details of which are summarized in Table 1. At the time when we initiated this study, an exhaustive literature review was completed to find longitudinal, within-host SARS-CoV-2 data sets that were either accessible through their published supplementary files or easily digitizable (clearly resolved data points). If unavailable directly from the published source, we digitized the data using the software WebPlotDigitizer (version 4.5) (Rohatgi, 2021). All data sets are in units of $\log_{10}$ copies per mL. For all data sets we fit to cohorts of individuals, that is, viral load measures were grouped and fit separately for each study, but not for each individual within a study.

The Goyal data set (Goyal et al., 2020), consisting of 25 individuals whose viral load time courses were collected from a mix of throat and nasopharyngeal swabs, was obtained from various sources: 11 hospitalized individuals from Singapore, median age 47 (31–73), symptom onset ranging from January 14–30, 2020 (Young et al., 2020); 9 hospitalized individuals from Munich, Germany, described as young to middle aged, symptom onset occurring in January, 2020 (Wölfel et al., 2020); 1 hospitalized individual from South Korea, aged 35 years old, symptom onset 18th of January, 2020 (Kim et al., 2020); 4 hospitalized individuals from Paris, France, median age 46, symptom onset mid-January, 2020 (Lescure et al., 2020). Measurement times in this data set correspond to days after first positive test. For the fits to this data set completed in this work, all values below the limit of 2 $\log_{10}$ copies/mL were considered below the detection threshold and censored.

The Néant data set (Néant et al., 2021) includes data obtained from 655 hospitalized individuals with a median age of 60. Viral load measurements were collected via nasal swabs from February 5 to April

Table 1
Summary of individual SARS-CoV-2 viral load cohorts used in this work.

Reference	Néant et al. (2021)	Jones et al. (2021)	Goyal et al. (2020)
Timeframe	Feb. 5–April 1, 2020	Feb. 24, 2020–April 2, 2021	Jan. 23–Feb 23, 2020
Location	France	Germany (Berlin)	Singapore, Germany, South Korea, France
Cohort size	655	4344	25
Number hospitalized	655	3475	25
Median age (range)	60 (48–72)	52 (29–74)	47
Acquisition method	Nasal	Sputum	Nasal & Sputum

1 2020 in France, where measurement times correspond to days since symptom onset.

The Jones data set (Jones et al., 2021) consists of viral load measurements from 4344 individuals, 3475 of which were hospitalized, with a median age of 52. Viral load measurements were acquired by sputum swabs from February 24, 2020, to April 2, 2021 in Berlin, Germany. Measurement times correspond to days since peak viral load. We note that Jones et al. (2021) report on a much larger data set consisting of 25,381 individuals, but for this work we only considered the subset of those ($n = 4344$) for which viral load time courses were available. Jones et al. (2021) report that 80% of the 4344 were hospitalized.

The measurement times in the Goyal data set, Neant data set, and Jones data sets are "days after first positive test", "days since symptoms onset", and "days since peak viral load", respectively. To estimate the initial time of infection, t_{inf} for each data set, the data points are shifted such that the first data point is at time 0. Therefore, t_{inf} is such that $t_{inf} < 0$.

2.2. Target-cell limited model

To model the within-host dynamics of SARS-CoV-2 viral shedding we use a target-cell limited model similar to that previously used to model influenza A (Sigal et al., 2018) and SARS-CoV-2 (Néant et al., 2021; Gonçalves et al., 2020). The model includes target cells (y_t), productively infected cells (y_B) capable of budding infectious virus (v) and non-infectious virus (w), and non-productively infected cells in the eclipse state, which is extended to include k eclipse stages (y_k). Target cells are assumed to be infected by infectious virus at rate α (mL d^{-1} copies^{-1}). Newly infected cells enter the eclipse phase. We consider a range of eclipse time distributions, each of which has a mean duration that is fixed to $\frac{1}{E}$ days. In particular, we extend the typical one-compartment model, which yields exponentially-distributed eclipse durations, to a linear chain of k eclipse stages (Hurtado and Kirosingh, 2019), yielding Erlang-distributed eclipse durations with shape parameter k. At the end of the eclipse phase, infected target cells enter the productively infected cell class, y_B. These cells have a constant loss rate D (d^{-1}) and produce virions at rate B ($\frac{\text{copies}}{d\ cell}$). Following the SARS-CoV-2 modelling work of Néant et al. (2021), we assume that a fraction, ϵ, of virions are infectious, and the remaining (1-ϵ) are non-infectious. Both infectious and non-infectious virions are cleared at a constant rate of C (d^{-1}). Similar to previous SARS-CoV-2 modelling work (Gonçalves et al., 2020), we include in our model a term for loss of infectious virus due to virus entry, $\alpha y_T v$. A schematic of this target-cell limited model is shown in Fig. 1a, and is given by the following system of ordinary differential equations:

$$\text{Target cells}: \quad \frac{dy_T}{dt} = -\alpha y_T v \tag{1a}$$

$$\text{Eclipse stage 1}: \quad \frac{dy_1}{dt} = \alpha y_T v - (D + kE) y_1 \tag{1b}$$

$$\text{Eclipse stage 2...k}: \quad \frac{dy_j}{dt} = kE y_{j-1} - (D + kE) y_j, \quad j = 2...k \tag{1c}$$

$$\text{Budding}: \quad \frac{dy_B}{dt} = kE y_k - D y_B \tag{1d}$$

$$\text{Infectious Virions}: \quad \frac{dv}{dt} = \epsilon B y_B - \alpha y_T v - C v \tag{1e}$$

$$\text{Non-infectious Virions}: \quad \frac{dw}{dt} = (1 - \epsilon) B y_B - C w. \tag{1f}$$

We also consider a reduced model with no eclipse phase; in this case newly infected cells instantaneously become productively infected (budding) cells. The no-eclipse model is:

$$\text{Target cells}: \quad \frac{dy_T}{dt} = -\alpha y_T v \tag{2a}$$

$$\text{Budding}: \quad \frac{dy_B}{dt} = \alpha y_T v - D y_B \tag{2b}$$

$$\text{Infectious Virions}: \quad \frac{dv}{dt} = \epsilon B y_B - \alpha y_T v - C v \tag{2c}$$

$$\text{Non-infectious Virions}: \quad \frac{dw}{dt} = (1 - \epsilon) B y_B - C w. \tag{2d}$$

2.3. Assumptions on initial conditions and parameter values

For each cohort fit, we assume an initial time of infection t_{inf} (days), where $t_{\text{inf}} \leq 0$, and where t_{inf} is determined through fitting with bounds on the fit of 0–14 days. Thus t_{inf} represents an expected initial time of infection for the cohort and the standard error in the estimate of this parameter may reflect heterogeneity in initial times across individuals. We assume an initial target cell concentration of 1.33×10^5 cells mL^{-1} as used in previous studies (Gonçalves et al., 2020; Néant et al., 2021; Baccam et al., 2006b). This value is obtained by assuming the upper respiratory tract contains 4×10^8 cells distributed evenly in a volume of 30 mL, and where only 1% of the cells express the ACE2 receptor associated with viral entry (Dinh et al., 2021). We assume an initial condition of one productively infected cell in the upper respiratory tract ($y_B = 1$ cell/30 mL). The initial condition for all y_j eclipse states is 0. The initial number of infectious and non-infectious virus particles is assumed to be 0.

We assume the proportion of produced infectious virions to be fixed at $\epsilon = 10^{-4}$, which was determined to be the upper bound in SARS-CoV-2 infection in non-human primates (Gonçalves et al., 2021); non-infectious virions are therefore produced at rate $(1-\epsilon)$. SARS-CoV-2 viral titres have been measured as soon as 2 h post infection (Agostini et al., 2018); as not all parameters in the model can be fit, we fix the mean eclipse duration to $1/E = 0.2$ days, which corresponds to viral production beginning, on average, 4.8 h after cell infection. For each cohort we fit the parameters α, B, C, and D. A summary of all parameter assumptions and initial conditions can be found in Table S1.

We note the lack of parameter assumptions regarding SARS-CoV-2 virion clearance, captured by parameter C, in this work. Previous SARS-CoV-2 target-cell limited modelling work typically fix C to 10 d^{-1} (Ke et al., 2022; Gonçalves et al., 2020; Néant et al., 2021; Marc et al., 2021; Gonçalves et al., 2021) or 15 d^{-1} (Goyal et al., 2020). In these previous studies, the justification for fixing C is not made explicit, and often the trail of references for justification lead to confusing justification for SARS-Cov-2. For example, Ref. Gonçalves et al. (2021) fix C to 10 d^{-1} citing consistency with human influenza virus data fits from Ref. Baccam et al. (2006c), despite the fact that Ref. Baccam et al. (2006c) find an average C of 3 d^{-1} ranging from 2.1–4.2 d^{-1} without delay, and 5.2 d^{-1} ranging from 2.2–13.5 d^{-1} with delay. Ref. Gonçalves et al. (2020), a study on humans with SARS-CoV-2, fix C = 10 d^{-1} citing consistency with Zika virus clearance in nonhuman primates (Best et al., 2017). However, Ref. Best et al. (2017) in turn fixed C to 10 d^{-1} in their work citing C = 10 d^{-1} had the lowest BIC

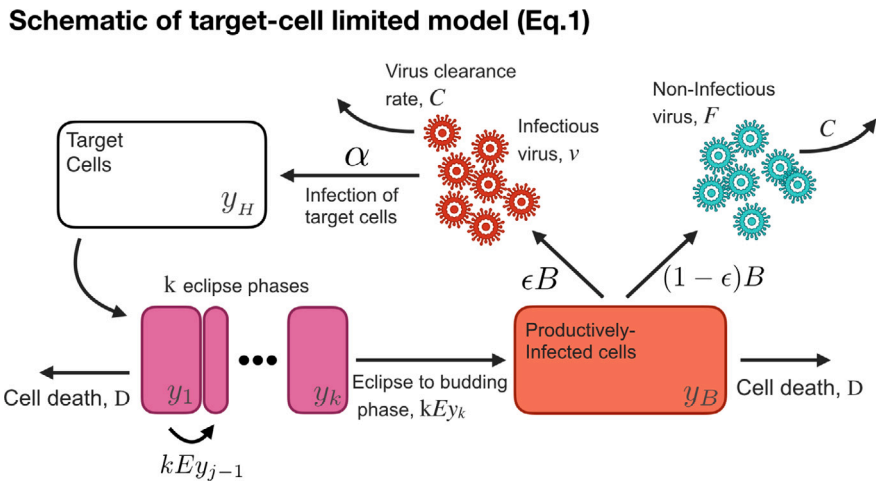

Fig. 1. Schematic of target-cell limited model described in Section 2.2.

when varied across the range 5–15 d^{-1}, thus, they perform an informed model-fit approach to estimate a physiologically reasonable value of C for Zika virus in order to fix that value in subsequent fits reported in the main text. We find no strong structural or practical identifiability arguments in the literature requiring C to be fixed when fitting to viral load data. Therefore, a secondary goal of this work is to determine how data resolution, e.g. whether or not peak or pre-peak dynamics are resolved, affect how well the parameter estimates are constrained to the data sets, and further, to determine if fixing C = 10–15 d^{-1} is reasonable for SARS-CoV-2 in humans.

2.4. Parameter estimation and fitting assessment

All fits to Eq. (1) were performed in Monolix 2020R1 (2020) (Version 2020R1) using non-linear mixed-effects models. Individual parameters for each data set are determined by the maximum likelihood estimator Stochastic Approximation Expectation–Maximization (SAEM), and all fits met the standard convergence criteria (complete likelihood estimator). For all data sets we fit the parameters α, B, C, D and t_{inf}, and all parameters were assumed to be log-normally distributed. Further details of the fits, including priors, population values, and random effects, are given in Table S1.

2.5. Sensitivity and error analysis

We report residual errors assuming a 'combined' error model, whereby the error term in the observation model is composed of a constant fitted term and a term proportional to the structural model (Monolix 2020R1, 2020).

We perform sensitivity analysis to characterize the response of model outputs to variation in the fitted parameters as well as the fixed parameter, E. Latin Hypercube Sampling (LHS) and Partial Rank Correlation Coefficient (PRCC) (McKay et al., 2000) are employed to study the effects of model outcomes on the peak value of each state variable.

An independent error analysis is also completed to complement the fit errors found by Monolix. Here we compute the mean standard error between the curve produced by the target-cell limited models and the Jones data set (Jones et al., 2021). For each set of fitted parameters, for each value of k, the mean standard error is computed by

$$\sigma_{SE} = \langle |(V_t - J(t))| \rangle , \tag{3}$$

where $V_t = \log[v(t) + w(t)]$ and $J(t)$ is the average value from the Jones data set at time t. To compute σ_{SE}, we bin the Jones data in 0.5 day intervals, where the data in each interval is averaged.

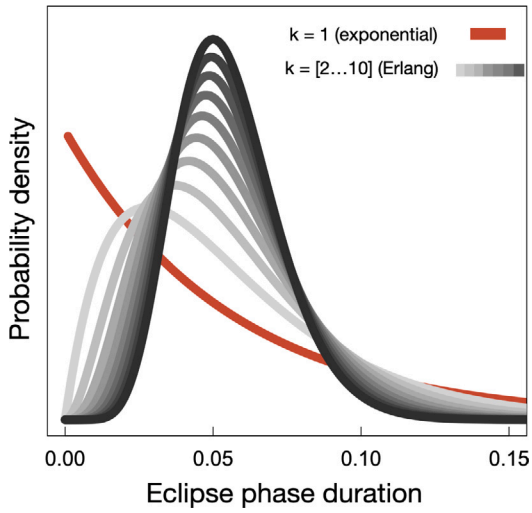

Fig. 2. Eclipse duration distributions are shown for $k = 1$ (exponential, red line) and $k = 2...10$ (Erlang, grey lines). For $k = 1$, a substantial fraction of cells have near-zero eclipse times; this issue is resolved for $k > 1$.

3. Results

3.1. Cohort-dependent variation in viral load dynamics

A schematic illustrating our model for $k > 0$ is shown in Fig. 1. Differences in eclipse duration distributions are shown in Fig. 2 for all k models. Fig. 3a depicts the timeline of the studies used in this work, which range from January 2020, to April 2021, and also vary both geographically and in cohort size (details provided in Table 1).

Examples of fits to all data sets are shown in Fig. 3b-d. In Fig. 3e we report, as a function of k, three different log-likelihood fit criteria: AIC (Akaike information criterion), BIC (Bayesian information criterion), and BICC (corrected Bayesian information criterion). Noting that a lower log-likelihood criterion suggests a more preferred model, we find non-monotonic behaviour in all criteria as a function of increasing k. The BIC, BICC, and AIC all increase from $k = 0$ to $k = 1$, and then decrease to a minimal plateau from $k = 2$ to $k = 8$. We find that from $k = 8$ to 10 the BIC and BICC values are approximately constant, while the AIC displays a slight increase at $k = 9$. Irrespective of the log-likelihood criterion used, the best fit occurs when $k = 3$. However values of all the log-likelihood parameters are within ≈2 units of the minimum log-likelihood for $k = 2$ through $k = 8$, suggesting that models

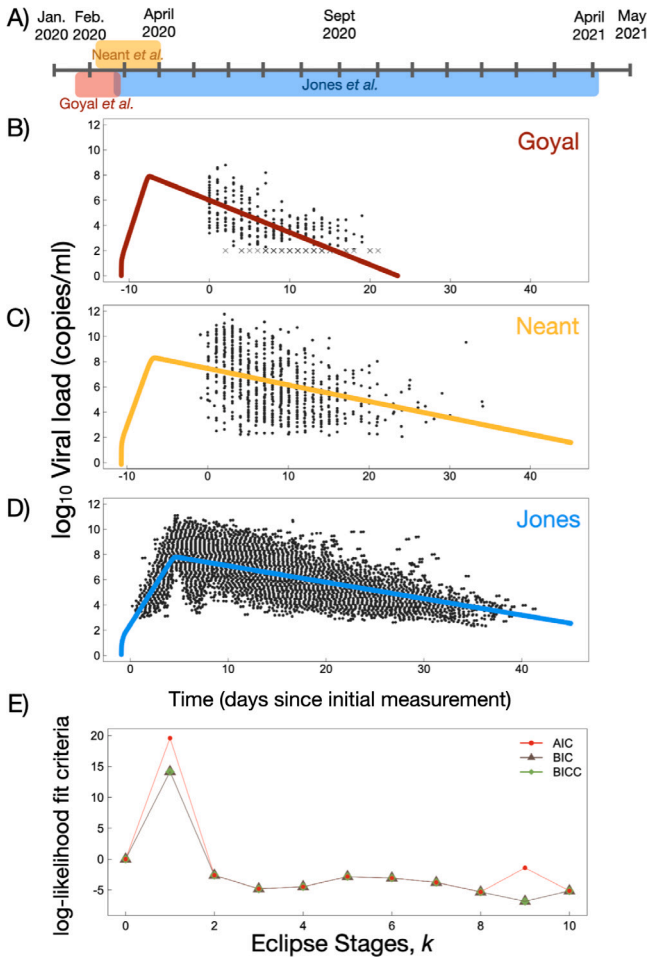

Fig. 3. (A) Timeline of viral load studies used in this work. Further details about each study can be found in Table 1. (B)-(D) $\log_{10}$ viral load and examples of cohort fits for each data set used in this work. (E) Log-likelihood criteria for best fit as a function of number of eclipse stages, k. The value of each criterion at $k = 0$ has been subtracted for visual comparison.

with two through eight eclipse stages cannot be rejected as being the most appropriate model to fit these data (see Discussion for further details).

In Fig. 4 we plot the best fit parameter values as a function of k for the Goyal data set, Jones and Néant cohorts, while Fig. S1 displays the estimated time of infection, t_{inf}. The error bars in Fig. 4 show the residual error for each parameter determined by the fit (Monolix 2020R1, 2020), and open symbols give the mean and standard deviation of best fit parameters across all accepted models ($k = 2...8$). The best fit values of each parameter for each data set, as well as the mean and standard deviation across all k values, are provided in Table S2.

A general conclusion from Fig. 4, consistent with the results from the log-likelihood criteria, is that best-fit parameter values for $k = 0$ and $k = 1$ can vary substantially from best-fit values obtained for $k \geq 2$. Focusing on the results from accepted models (open symbols) we see that the estimated budding rate, ϵB, is fairly similar across cohorts, and is relatively insensitive to k for $k \geq 2$. The best-fit values of α and D are also relatively robust to changes in k for $k \geq 2$, but vary substantially across the different cohorts. Finally, the parameter C shows substantial variability among cohorts, and within each cohort shows a high sensitivity to k.

The estimated initial infection times, t_{inf}, for each model are provided in Fig. 1. Little variability is found amongst the Goyal and Jones data sets, however, the estimated t_{inf} for the Goyal data sets are consistently near the allowed boundary for t_{inf} at 14 days prior to the initial measurement. t_{inf} for the Neant data set is found to vary between 11 and 13.5 days prior to the initial data point.

A Partial Rank Correlation Coefficient sensitivity analysis is performed to assess how model fit parameters affect the peak response from each state variable, the result of which is shown in Figure S5. We find the sensitivity analysis to reveal intuitive trends based on the model structure for all fitted parameters. LHS parameters close to $+1/-1$ indicate strong influence on the outcome measure, where negative values suggest the parameter is inversely proportional to the outcome measure, and PRCC values whose magnitude is greater than 0.5 are considered important (GomeroBoloye, 2021). We find peak v and w have positive PRCC values of $\sim$1 for the budding rate, B, and less than -0.5 PRCC values for the clearance and cell removal rates C and D, respectively. We also find the y_B peak to have a PRCC value of less than -0.5 for the cell removal rate, D.

To qualitatively visualize parameter influence on viral load estimates, we vary each parameter around the mean-determined values across all accepted fits, keeping each parameter within physiologically reasonable bounds. The result of which is shown in Fig. 6.

3.2. R_0 Analysis

The basic reproduction number, R_0, is defined by the average number of secondary infected cells resulting from a single infected cell in a population of susceptible cells at the beginning of infection (Diekmann and Heesterbeek, 2000; Diekmann et al., 2010; Heffernan et al., 2005). Following the method of Diekmann and Heesterbeek (2000) and Diekmann et al. (2010), we derive R_0 for our target-cell limited model (Eq. (1)) for k eclipse phases ($k \geq 1$) assuming initial disease-free equilibrium conditions (see supplementary material for calculations of the disease-free equilibrium). For R_0 corresponding to Eq. (1) we use the notation $R_0^{k>0}$. We find $R_0^{k>0}$ to be

$$R_0^{k>0} = \frac{\epsilon\alpha B y_{T_0}}{D(\alpha y_{T_0} + C)} \frac{(kE)^k}{(D + kE)^k} = \frac{\epsilon\alpha B y_{T_0}}{D(\alpha y_{T_0} + C)} S(k) \tag{4}$$

where $S(k)$ denotes the probability that an infected cell survives all k eclipse stages, since the probability of maturing through a single eclipse stage rather than dying is given by $kE/(kE + D)$. In the limit of $k = 0$, corresponding to Eq. (2), $R_0^{k=0}$ is found to be

$$R_0^{k=0} = \frac{\epsilon\alpha B y_{T_0}}{D(\alpha y_{T_0} + C)}. \tag{5}$$

Thus, $R_0^{k>0} = R_0^{k=0} S(k)$. Therefore, the effect of the eclipse phase on the basic reproduction number is simply to reduce R_0 by S(k).

Fig. 7a displays $R_0^{k=0}$ and $R_0^{k>0}$ as a function of the number of eclipse stages, k, for all three data sets. We find the Néant and Jones data sets to have estimated R_0 values of $\sim$10 and $\sim$17.5 across all accepted model fits ($k = 2...8$). As reflected in the best-fit parameter estimates, the use of $k = 0$ or $k = 1$ can result in markedly different predictions for R_0; this is particularly striking in the Néant data set. The R_0 estimate obtained for the Goyal data set shows substantial sensitivity to the choice of k, which may be a result of the small cohort size, and limited number of data for this study.

To gain further insight into the influence of the fitted parameters α, B, C, and D on R_0 with increasing k, we compute $R_0^{\infty} = \lim_{k\to\infty} R_0^{k>0}$. Using a straightforward application of L'Hôpital's rule, we obtain

$$R_0^{\infty} = \lim_{k\to\infty} R_0^{k>0} = R_0^{k=0} \lim_{k\to\infty} S(k) = R_0^{k=0} \lim_{k\to\infty} \frac{(kE)^k}{(D + kE)^k} = R_0^{k=0} e^{-\frac{D}{E}}. \tag{6}$$

Fig. 7b shows the approach of $S(k)$ to the limiting value of $e^{-\frac{D}{E}}$ given parameter values D and E of 0.32 and 5 d^{-1}, respectively. This figure shows that as the number of eclipse stages increases, $S(k)$ monotonically decreases towards the $e^{-\frac{D}{E}}$ limit.

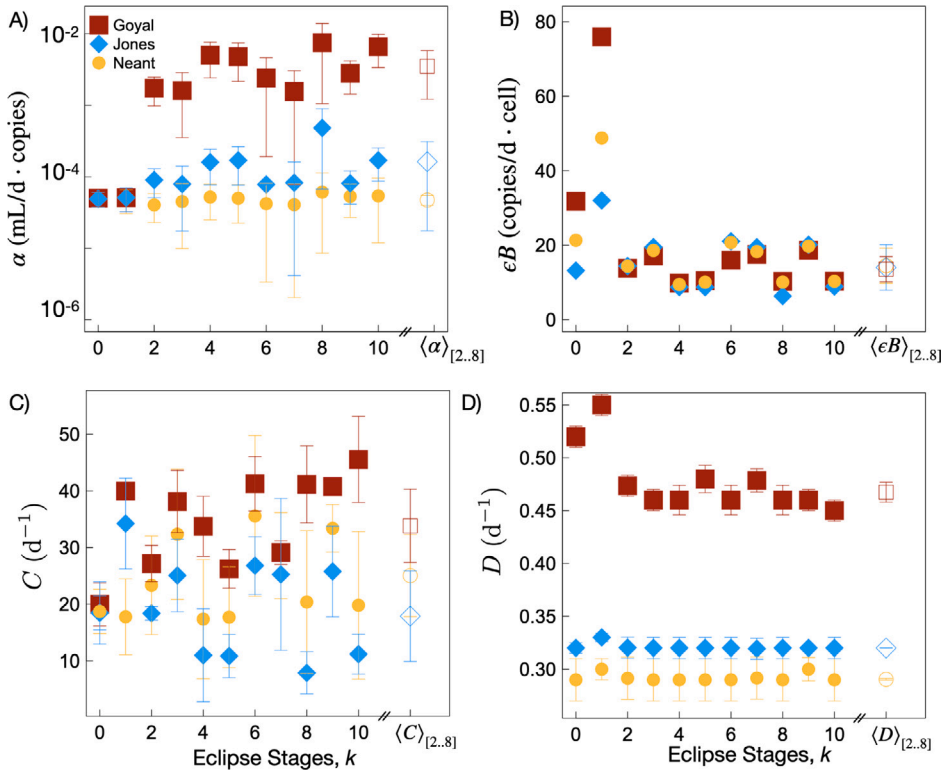

Fig. 4. Best-fit parameter values for the Goyal, Néant and Jones data sets as a function of the number of eclipse stages, k. Error bars are the residual error determined through the fit. Open symbols (on the right) of each plot are the mean and standard deviation for each parameter value across all accepted fits ($k = 2...8$). (A) The per-target cell attachment rate, α. (B) The infectious virion budding rate, ϵB. (C) The virion clearance rate, C, and (D) The cell removal rate, D.

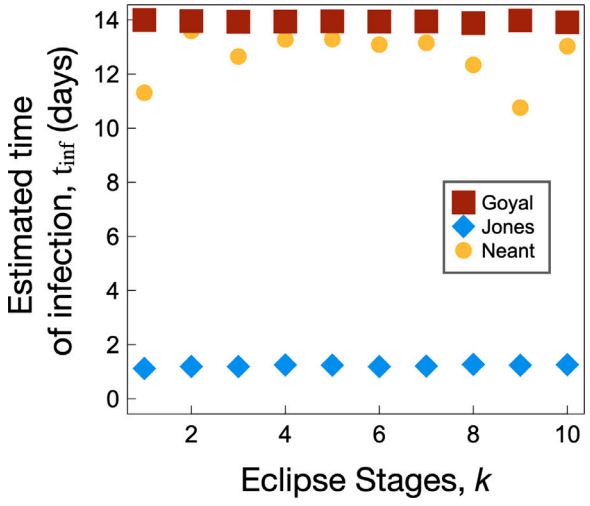

Fig. 5. Estimated time of infection, t_{inf}, for the Neant, Goyal, and Jones data sets for all k eclipse stages.

We point to the narrow y-axis scale in Fig. 7b, showing that, for the parameter values illustrated here, varying the number of eclipse stages over a large range has a negligible effect on R_0. In particular, fixing $E = 5$ d^{-1}, and taking $D = 0.29$, 0.32, or 0.48 as estimated for the Néant, Jones and Goyal studies respectively (Table S2), changing k from 0 to the limit as $k \to \infty$, we find a maximum percent reduction in R_0 of 5.3, 5.8 and 8.3% in these three studies, respectively.

Although R_0 is relatively insensitive to k at fixed parameter values, we also note that as k changes, the best-fit parameter values may also change. Nonetheless as seen in Fig. 7a, estimates for R_0 are relatively insensitive to k for the Jones and Néant data sets across the accepted models ($k = 2...8$).

In Fig. 8 we plot R_0^∞ as a function of α, ϵB, C, and D. Coloured regions highlight the standard deviation of parameter estimates across all models for best-fit parameters for each of the three data sets, while the solid coloured vertical lines are the mean parameter estimates. The steepness of the curve in each region thus reflects the sensitivity of R_0 to changes in each parameter. For example we find that the best-fit α values from the Goyal cohort lie in a region of parameter space where changes in α have little effect on R_0, whereas slight changes in the α value estimated for the Néant cohort may appreciably affect R_0 (Fig. 8a). Clearly R_0^∞ (Eq. (6)) has a linear dependence on B with constant slope. Thus, variations in B for any study would lead to a similar shift in R_0 (Fig. 7b). R_0^∞ monotonically decreases as a function of both C and D; the Goyal fits are found to have the highest values for both parameters, whereas the Néant and Jones fits have quite similar values for all k. Thus, this analysis suggests that the larger values of R_0 estimated for the Goyal cohort may be largely attributed to the larger α values estimated for that data set, as compared to the Néant and Jones data sets (Fig. 4a).

4. Discussion

We employed a series of target-cell limited models accounting for infected cell budding, a loss rate of infected cells, differing eclipse stage dynamics, and infectious and non-infectious virion production and clearance. We fit these models to three previously published SARS-CoV-2 viral load cohorts comprised of mostly hospitalized individuals: Néant et al. (2021) (n = 655), Jones et al. (2021) (n = 4344) and Goyal et al. (2020) (n = 25). We varied the number of eclipse stages, k, from 0 (Eq. (2)) to 1–10 (Eq. (1)), where all fits consist of the same number of fitted parameters, and begin with similar priors (See Table S1 for this information). All fits were completed in Monolix 2020R1 (2020)

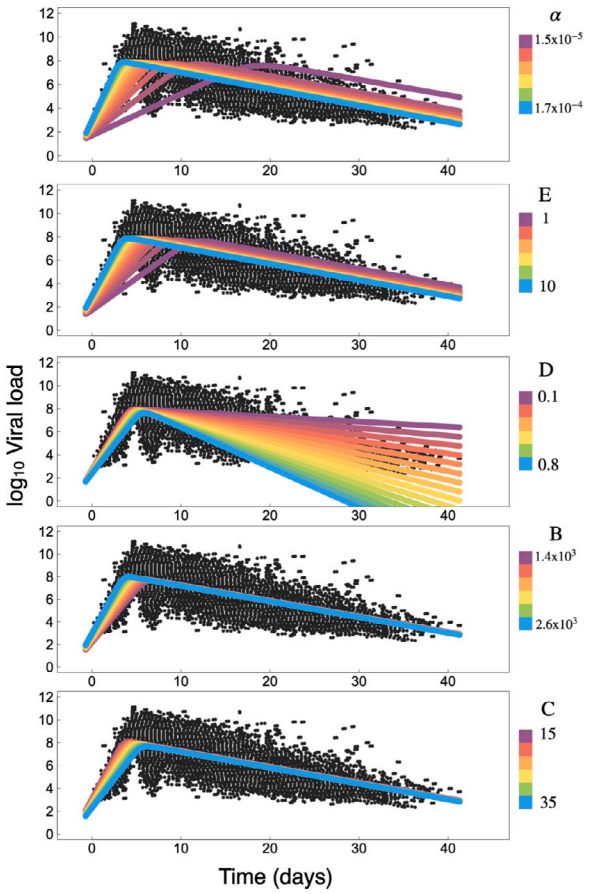

Fig. 6. For illustrative purposes, parameters for model Eq. (1) were varied around the mean values obtained for Jones et al. (2021) to show their relative influence over the viral load model dynamics. We can see, for example, that the time-to-peak is largely influenced by α and E, the dynamics of the rise to the peak are influenced by α, E, B and C, while the slope of the viral load from peak to complete clearance is determined by D.

which employs the SAEM algorithm, and all fits met the log-likelihood convergence criteria (see Methods for details).

Eclipse dynamics capture the inherent delay between the moment that a virion infects a target cell and the time at which the cell begins to bud new virions. A single eclipse compartment ($k = 1$) yields an exponentially-distributed eclipse duration, and is often implemented in in-host models as the simplest way to incorporate an eclipse stage (see Perelson and Ke (2021)). This "simplest approach" to model development is an important guiding principle, particularly when faced with noisy, real-world clinical data. Increasing the number of freely fit parameters can lead to overfitting and may potentially introduce identifiability issues; interpreting the biological consequences in the resulting parameter fits becomes more difficult or impossible. Although extending the model from $k = 0$ to $k = 1$ involves introducing a new parameter – the eclipse rate E – we fixed this parameter based on previous SARS-CoV-2 literature (Agostini et al., 2018) for all $k > 0$ to allow for a more fair comparison between models for $k = 0$ and $k > 0$ and to avoid structural identifiability issues (discussed below). Thus, we fit the same number of parameters, each with consistent priors, for all models.

While the lowest AIC obtained among a group of candidate models (AIC_{min}) indicates the most preferred model, the amount by which the AIC of a particular model exceeds this minimum ($\Delta AIC = AIC - AIC_{min}$) is a key parameter in accepting or rejecting candidate models. A value of ΔAIC of less than 2 reflects 'equal support' for the two models. ΔAIC of 2–10 is considered 'substantial support' for the less preferred model, while ΔAIC of 10 or more reflects 'essentially no support' (Burnham and Anderson, 2004). For our models, all three log-likelihood criteria increase substantially from $k = 0$ to $k = 1$, followed by a decrease to a near-equivalent preference for $k \geq 2$. We find that $k = 3$ is the most preferred model with the lowest AIC (Fig. 3e). Values of ΔAIC for $k = 2...10$ (excluding 3) vary between 0.4 ($k = 4$) and 3.4 ($k = 9$). Thus, although $k = 3$ results in the lowest AIC, all $k > 1$ models considered in this study are either considered 'equivalently preferred' or have 'substantial support' as an acceptable model. For $k = 0$, ΔAIC = 4.8, suggesting that the inclusion of an eclipse phase is justified in fitting these data. However for $k = 1$, ΔAIC = 24.4; thus the use of a single eclipse compartment (exponentially-distributed eclipse duration) can be strongly rejected.

The finding that models containing $k > 1$ eclipse stages are preferred over $k = 1$ suggests that the eclipse duration is not best-described by an exponential distribution; rather, for $k > 1$ in Eq. (1) the eclipse stage duration is described by an Erlang distribution identified by its shape and scale, with a shape parameter greater than one. For illustrative purposes, in Fig. 2 we plot the distribution of the eclipse duration for $k = 1$ through to $k = 10$. One can see that the eclipse duration distribution for $k = 2$ resolves the major issue raised previously in modelling SHIV (Kakizoe et al., 2015), namely, that with an exponential distribution, many cells instantly begin budding at the moment of virion attachment to the target cell. For $k > 1$, this issue is resolved as the probability of an eclipse duration of zero is not possible. We conclude that the simplest model that provides a statistically acceptable fit to the data has a shape parameter of at least $k = 2$, and find the strongest support for $k = 3$.

Our finding that a target-cell limited model with $k > 1$ has more support compared to that with $k = 1$ mirrors findings for model fitting of other in-host infections (Beauchemina et al., 2012; Rong et al., 2007; Maziane et al., 2015; Kakizoe et al., 2015). For example, recent rigorous modelling of the within-host kinetics of *Orthohantavirus* also concluded that $k > 1$ yielded more preferred models, where $k = 3$ was also found to have the strongest support (Adams et al., 2022). Further, two-parameter distributions, such as Weibul, are considered more appropriate when stochastically modelling eclipse waiting times, where eclipse waiting times have been shown to have a significant affect on viral co-infection (Vafadar et al., 2021).

Despite these strong arguments for using $k > 1$ eclipse stages, we also analytically explored how varying k alters R_0. We found that, as the number of eclipse stages k increased, R_0 converged to $R_0^{k=0} e^{-\frac{D}{E}}$. We also found that, for our model parameter values for D and E corresponding to the Jones, Néant, and Goyal data sets, the maximum decrease in R_0 as $k \to \infty$ is ~5%–8%. Thus previous studies of SARS-CoV-2 that assume a single eclipse compartment ($k = 1$) may see little impact on estimated R_0 values if they were to instead use $k > 1$ eclipse stages (assuming the values of other fitted parameters remain constant). Indeed, where we consider fitting models consisting of one to ten eclipse stages, for our Jones fits (where $n = 4344$), we find very little variability in R_0 across all k eclipse stages (Fig. 7a), and with the exception to $k = 1$, we find little variability with k in R_0 estimated for the Néant data ($n = 655$) as well. We discuss the highly variable R_0 estimated for the Goyal ($n = 25$) data set in more detail below.

The Néant data set consists of 655 SARS-CoV-2 positive hospitalized individuals with samples acquired between February and April of 2020 in France. The Jones data set consists of 4344 individuals from Berlin, 80% hospitalized, with samples acquired over a much longer time frame from February 2020 to April 2021. Thus, the Jones data set, consisting of more individuals, will not only have captured greater heterogeneity in SARS-CoV-2 in-host viral load dynamics (such as clearance and peak dynamics) but will also reflect a myriad of variants that swept through Germany over the course of 2020–2021. While the mean R_0 we estimate using the Néant data set was 9.4, we find the mean R_0 for the Jones data set to be 17.1. Referring to the best-fit parameter estimates in Fig. 4, we see that the higher R_0 computed for

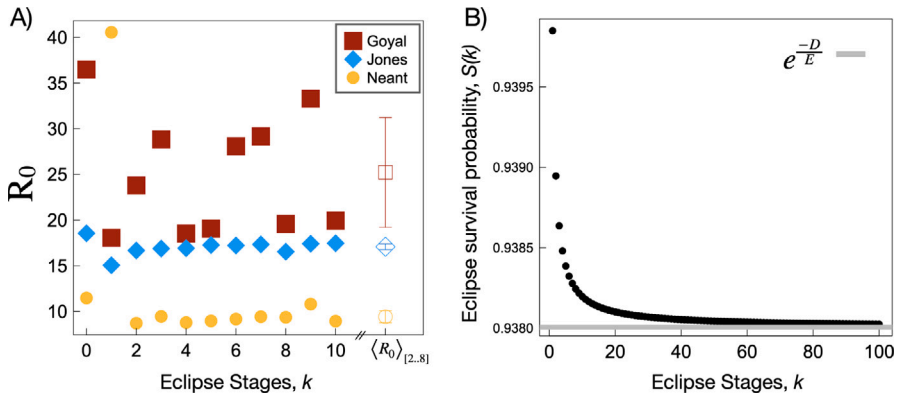

Fig. 7. (A) R_0 as a function of k for the best-fit parameter values for each data set. Open symbols (on the right) show the mean and standard deviation of R_0 across all accepted fits ($k = 2...8$). (B) The probability of surviving the eclipse phase, $S(k)$ versus the number of stages in the eclipse phase, k. $S(k)$ approaches the limit $e^{-\frac{D}{E}}$ as $k \to \infty$.

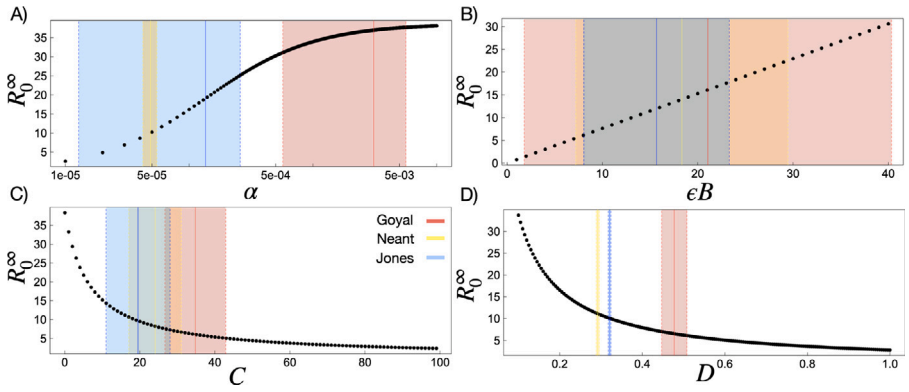

Fig. 8. (A-D) R_0^∞ (Eq. (6)) as a function of α, ϵB, C, and D, respectively. Coloured regions correspond to the standard deviation of parameter estimates across all models, while the solid vertical lines are the mean parameter values across all models.

the Jones fits is driven in part by a higher estimate of α for this data set. This higher attachment rate might be related to the increased infectivity of variants that emerged later in 2021 (Baric, 2020; Cai et al., 2021).

There are two types of identifiability concerns: structural and practical. Structural identifiability methods are used to determine whether each model parameter has an effect on the model output, whereas practical identifiability attempts to quantify whether the estimated model parameters are well-constrained by the various data sets to which they are being fit (Sher et al., 2022). For this work we were particularly interested in exploring the reliability of model parameter estimation from low resolution data, where initial and peak dynamics may not have been captured. Consider the Goyal data set, which includes 25 individuals; times in these data correspond to days after a first positive test. It is known that symptom onset is correlated with peak infectious load where for SARS-CoV-2 symptoms have been shown to begin within 1 day of peak viral load (Stankiewicz Karita et al., 2021). Typically individuals will not seek testing until after symptoms have begun, thus, the Goyal data set likely captures late-stage dynamics, past the peak of infection; this conjecture is supported by the fact that the maximum viral load in this data set is considerably lower than that observed in the other data sets. This limited data resolution poses an issue when trying to estimate parameters, such as the budding, clearance and per-target cell attachment rate, which are particularly important during the early-stage dynamics, as well as the initial time of infection. To illustrate the importance of sampling timescales on parameter estimation, we varied parameters for model Eq. (1) around the mean values estimated for Jones et al. (2021) to show their relative influence over the viral load dynamics (see Fig. 6). We observe that parameters B and C have a very similar influence over the slope of the initial rise in viral load. Similarly, E and α both influence the time to peak. Finally, we note that the post-peak slope remains at the same slope when any of these four parameters are changed; only D changes the slope of viral load decay. These conclusions are mirrored in the PRCC analysis (Fig.S5), which demonstrates that B, C and E strongly affect the peak viral load, while parameter D influences the peak density of budding cells.

If initial and peak infection dynamics are not present, it is therefore difficult to estimate parameters without also considering parameter bounds and literature-informed priors: there are considerable practical identifiability concerns for all parameters that govern the rise towards the peak, and peak placement in time. For data sets that do not capture the peak viral load, valid estimates of the parameter D should be possible, but the other parameters may not be uniquely identifiable. Practical identifiability issues lead to parameter variations that lead to considerable variation in R_0 values, as particularly evident for the Goyal data set fits, where R_0 range from 18 to 36.5 as k changes (see Fig. 7). Such variation in fits from low-resolution data have been reported in a previous TEIV study comprised of 13 SARS-CoV-2-positive individuals (Gonçalves et al., 2020). Gonçalves et al. (2020) determine an R_0 of 8.6, but also report a large range of values of 1.9–17.6. We propose that the large range of R_0 values is due to the absence of peak viral load data leading to a myriad of practical identifiability issues amongst the fitted parameters.

Are the parameters of our model uniquely identifiable in principle, given enough data? To address this question, we non-dimensionalize Eq. (1) (Eqs. S16). We find, in the limit of infinite data, only three out of four of the parameters ϵB, C, D, and E are independently identifiable where the ratios $\frac{\epsilon B}{C}$, $\frac{D}{C}$, and $\frac{E}{C}$ can be determined. However, in order to fit the reduced system of equations to data, both the time scaling (which involves C) and the viral load scaling (which involves α) are necessary. Thus, all the parameters are, in principle, meaningful to the

data fitting performed. To improve precision given limited data, one approach is to place bounds, or simply fix, particular parameters based on the relevant literature. In this work, for example, we limited t_{inf} to a maximum of 14 days, similar to Néant et al. (2021), and also fixed the mean eclipse duration, $\frac{1}{E}$. Placing bounds on t_{inf} implicitly places bounds on parameters that govern the rise to the peak, such as B and C (See Fig. 6). Taken altogether, Figs. 6, 4, and our parameter reduction analysis suggest that C is particularly hard to identify in these data, and cannot be quantified with precision particularly with both limited data capturing post-peak dynamics and while also seeking to fit B and D. We were therefore motivated to study how well we can reliably determine C from various data sets with varied pre and post-peak resolution, and to compare our results with previous fitted values from both the SARS-CoV-2 and influenza literature.

Given the above concerns raised with both practical and structural identifiability in the model fit, we next motivate our findings for the clearance rate, C (Fig. 4C). We find the mean C values across our accepted fits ($k > 1$) to be 34.8 ± 8.1, 18.5 ± 8.5, and 24.1 ± 7.0 for the Goyal, Jones, and Neant data sets, respectively. Pawelek et al. (2012) fit a TEIV model to influenza viral load data where peak-viral load dynamics were resolved in $n = 6$ horses, and fit an average C of 15 d^{-1} ranging 5.8–20 d^{-1}. Similarly, Baccam et al. (2006c) fit a TEIV model to influenza viral load data where peak-viral load dynamics were resolved in $n = 6$ humans and find an average C of 5 d^{-1} ranging from 2.2–13.5 d^{-1}. Thus, a fixing C to 10 or 15 d^{-1} is not unreasonable. Where the Jones data set contains a full profile of viral load dynamics, particularly peak and pre-peak resolution, we believe the C estimate of 18.5 ± 8.5 to be physiologically reasonable estimate for SARS-CoV-2. Our full range of viral clearance rates across all fits are also comparable to HIV-1 and HCV viral load clearance in humans, which has been found to broadly range from 9.1–36 d^{-1} and 5.5–9.9 d^{-1} for HIV-1 and HCV, respectively (Ramratnam et al., 1999).

We next compare and discuss our estimated time of infection, t_{inf} (Fig. 5, Table S2). A reasonable t_{inf} can be inferred by computing the total time of infection, estimated by the difference in estimated time of initial viral load detection and the time at which viral load drops below the detection threshold. In the Jones data set, where viral load data is highly resolved, the total time of infection can be as long as 40 days (Fig. 3, Jones data). We can also get an estimate of infection times from the literature. Time to viral clearance from infection (defined around time of symptom onset) through to first negative PCR test has been found to be 20(17–21) days amongst children and 23(20–15) days in adults (Sandoni et al., 2022). In another study using viral load to estimate incubation periods, t_{inf} was found to vary considerably from 2.65 to 12.99 days, with the total course of the infection (by a qualitative estimate from Ref. Ejima et al. (2021), Fig.2) to be approximately 30–35 days. The estimated total time of infection from our Goyal and Neant fits, where t_{inf} is estimated from post-peak dynamics, are approximately 30 ± 1 and 45 ± 3 days, respectively, across all k fits. These total infection times compare well to expected values from the literature. Our total infection times differ from those previously published by Goyal et al. (2020) who find t_{inf} to vary from 1.32 to −7.58 days (demonstrating a total absolute range of 8.9 days). Differences between our t_{inf} estimates as well as variability within those estimated by Goyal et al. outline practical identifiability concerns when fitting to low-resolved data, and may further be exacerbated by differences in model structure. We also note that while the total time of infection predicted for the Neant data set is reasonable, this is achieved in the model because t_{inf} is estimated to be 11–13.5 prior to symptom onset. This suggests, that t_{inf} must be more strictly bounded, or fixed, in the Neant data set where peak dynamics are not resolved. As mentioned in the methods, we bound t_{inf} to be between 0 and 14 days, as done in previous modelling work (Néant et al., 2021). This boundary is based on previous work which found the median incubation period of SARS-CoV-2 in humans to be 5.1 days, with 97.5% of individuals developing symptoms within 11.5 days (Lauer et al., 2020). Although Néant et al. (2021) determine their best-fit (lowest BIC) t_{inf} to be 4.8 days, here, we find for the Neant data set a value closer to 11 days. Since $t = 0$ in this dataset corresponds to the time of symptom onset, this would imply an ∼11 day delay between initial infection and symptom onset for this cohort, which is still physiologically reasonable based on previous literature (Lauer et al., 2020), however, far from the median value of 5.1 days. We note, however, that the time between t_{inf} and our predicted peak time is approximately 5 days; the peak however does not align with 'symptom onset'. We believe this result again suggests t_{inf} must be more tightly constrained if it is to be fit for data lacking viral load peak resolution.

While in-host modelling studies typically report residual errors (sensitivity of parameter estimates to measurement error), here we also carefully investigated the sensitivity of parameter estimates to model structure (Fig. 4). We also examined the sensitivity of predicted time courses (Fig. 6), the compound parameter R_0 (Fig. 8), the standard error between model results and data (Fig. S2), and peak densities (Fig. S3) to variations in parameter estimates. These sensitivity analyses form a critical context for the interpretation of SARS-CoV-2 within-host parameter estimates, and should help to inform future modelling as more data become available. We conclude that cohort-dependent variation in viral load dynamics can be caused by the quality of the data set being fit, namely, whether or not peak and pr-peak viral load trajectory information is present. Inherent differences in virus infection dynamics amongst infected individuals is then very difficult to quantify as many *a priori* assumptions must be made to limit or fix the model parameters. Comparing fitted parameters across studies is then difficult due to practical identifiability concerns with many parameters in the TEIV model when peak viral load is not present. Furthermore, these practical identifiability issues lead to difficulties reproducing previous model results, despite employing similar model structures to similar data sets.

CRediT authorship contribution statement

Chapin S. Korosec: Conceptualization, Formal analysis, Methodology, Investigation, Visualization, Writing – original draft, Writing – review & editing. **Matthew I. Betti:** Conceptualization, Methodology, Funding acquisition, Writing – review & editing. **David W. Dick:** Methodology, Writing – review & editing. **Hsu Kiang Ooi:** Methodology, Writing – review & editing. **Iain R. Moyles:** Conceptualization, Methodology, Funding acquisition, Writing – review & editing. **Lindi M. Wahl:** Conceptualization, Methodology, Funding acquisition, Supervision, Writing – original draft, Writing – review & editing. **Jane M. Heffernan:** Conceptualization, Methodology, Funding acquisition, Supervision, Project administration, Writing – review & editing.

Declaration of competing interest

The authors declare that they have no known competing financial interests or personal relationships that could have appeared to influence the work reported in this paper.

Acknowledgements

We thank Jeremie Guedj, Samaneh Gholami, and the Canadian In-host Modelling group for fruitful discussions. This research is supported by NSERC Discovery, Canada Grants (JMH, LMW, IRM, MIB), CIHR-Fields COVID Modelling Task Force, Canada(JMH), and an NRC Pandemic Response Challenge Program, Canada Grant (JMH, HKO). CSK acknowledges NSERC PD, Canada funding.

Appendix A. Supplementary data

Supplementary material related to this article can be found online at https://doi.org/10.1016/j.jtbi.2023.111449.

References

Adams, A., Murphy, Q.M., Dougherty, O.P., Sawyer, A.M., Bai, F., Edholm, C.J., Williams, E.P., Allen, L.J.S., Jonsson, C.B., 2022. Data-driven models for replication kinetics of Orthohantavirus infections. Math. Biosci. 349, 108834. http://dx.doi.org/10.1016/j.mbs.2022.108834.

Agostini, M.L., Andres, E.L., Sims, A.C., Graham, R.L., Sheahan, T.P., Lu, X., Smith, E.C., Case, J.B., Feng, J.Y., Jordan, R., Ray, A.S., Cihlar, T., Siegel, D., Mackman, R.L., Clarke, M.O., Baric, R.S., Denison, M.R., 2018. Coronavirus susceptibility to the antiviral remdesivir (GS-5734) is mediated by the viral polymerase and the proofreading exoribonuclease. MBio 9 (2), http://dx.doi.org/10.1128/mBio.00221-18.

Arino, J., Bajeux, N., Portet, S., Watmough, J., 2020. Quarantine and the risk of COVID-19 importation. Epidemiol. Infect. 148.

Baccam, P., Beauchemin, C., Macken, C.A., Hayden, F.G., Perelson, A.S., 2006a. Kinetics of influenza A virus infection in humans. J. Virol. 80 (15), 7590–7599.

Baccam, P., Beauchemin, C., Macken, C.A., Hayden, F.G., Perelson, A.S., 2006b. Kinetics of Influenza A Virus Infection in Humans. J. Virology 80 (15), 7590–7599. http://dx.doi.org/10.1128/jvi.01623-05.

Baccam, P., Beauchemin, C., Macken, C.A., Hayden, F.G., Perelson, A.S., 2006c. Kinetics of Influenza A Virus Infection in Humans. J. Virol. 80 (15), 7590–7599. http://dx.doi.org/10.1128/jvi.01623-05.

Baric, R.S., 2020. Emergence of a Highly Fit SARS-CoV-2 Variant. N. Engl. J. Med. 383 (27), 2684–2686. http://dx.doi.org/10.1056/NEJMcibr2032888.

Beauchemin, C.A., Miura, T., Iwami, S., 2017. Duration of SHIV production by infected cells is not exponentially distributed: Implications for estimates of infection parameters and antiviral efficacy. Sci. Rep. 7 (1), 1–13. http://dx.doi.org/10.1038/srep42765.

Beauchemina, C.A., McSharry, J.J., Drusano, G.L., Nguyen, J.T., Went, G.T., Ribeiro, R.M., Perelson, A.S., 2012. Modeling Amantadine Treatment of Inuenza A Virus In Vitro. J. Theoret. Biol. 254 (2), 439–451. http://dx.doi.org/10.1016/j.jtbi.2008.05.031.Modeling.

Best, K., Guedj, J., Madelain, V., De Lamballerie, X., Lim, S.Y., Osuna, C.E., Whitney, J.B., Perelson, A.S., 2017. Zika plasma viral dynamics in nonhuman primates provides insights into early infection and antiviral strategies. Proc. Natl. Acad. Sci. USA 114 (33), 8847–8852. http://dx.doi.org/10.1073/pnas.1704011114.

Betti, M., Abouleish, A.H., Spofford, V., Peddigrew, C., Diener, A., Heffernan, J.M., 2021a. COVID-19 vaccination and healthcare demand. MedRxiv.

Betti, M., Bragazzi, N.L., Heffernan, J.M., Kong, J., Raad, A., 2021b. Integrated vaccination and non-pharmaceutical interventions based strategies in Ontario, Canada, as a case study: a mathematical modelling study. J. R. Soc. Interface 18 (180), 20210009.

Betti, M.I., Heffernan, J.M., 2021. A simple model for fitting mild, severe, and known cases during an epidemic with an application to the current SARS-CoV-2 pandemic. Infect. Dis. Model. 6, 313–323.

Burki, T., 2020. The indirect impact of COVID-19 on women. Lancet Infect. Dis. 20 (8), 904–905.

Burnham, K.P., Anderson, D.R., 2004. Multimodel inference: Understanding AIC and BIC in model selection. Sociol. Methods Res. 33 (2), 261–304. http://dx.doi.org/10.1177/0049124104268644.

Cai, Y., Zhang, J., Xiao, T., Lavine, C.L., Rawson, S., Peng, H., Zhu, H., Anand, K., Tong, P., Gautam, A., Lu, S., Sterling, S.M., Walsh, R.M., Rits-Volloch, S., Lu, J., Wesemann, D.R., Yang, W., Seaman, M.S., Chen, B., 2021. Structural basis for enhanced infectivity and immune evasion of SARS-CoV-2 variants. Science 373 (6555), 642–648. http://dx.doi.org/10.1126/science.abi9745.

Challenger, J.D., Foo, C.Y., Wu, Y., Yan, A.W., Marjaneh, M.M., Liew, F., Thwaites, R.S., Okell, L.C., Cunnington, A.J., 2022. Modelling upper respiratory viral load dynamics of SARS-CoV-2. BMC Med. 20 (25), http://dx.doi.org/10.1186/s12916-021-02220-0.

Childs, L., Dick, D.W., Feng, Z., Heffernan, J.M., Li, J., Röst, G., 2021. Modeling waning and boosting of COVID-19 in Canada with vaccination. MedRxiv http://dx.doi.org/10.1101/2021.05.18.21257426.

Diekmann, O., Heesterbeek, J.A.P., 2000. Mathematical Epidemiology of Infectious Diseases: Model Building, Analysis and Interpretation, Vol. 5. John Wiley and Sons.

Diekmann, O., Heesterbeek, J.A., Roberts, M.G., 2010. The construction of next-generation matrices for compartmental epidemic models. J. R. Soc. Interface 7 (47), 873–885. http://dx.doi.org/10.1098/rsif.2009.0386.

Dinh, H.Q., Pan, F., Wang, G., Huang, Q.-F., Olingy, C.E., Wu, Z.-Y., Wang, S.-H., Xu, X., Xu, X.-E., He, J.-Z., Yang, Q., Orsulic, S., Haro, M., Li, L.-Y., Huang, G.-W., Breunig, J.J., Koeffler, H.P., Hedrick, C.C., Xu, L.-Y., Lin, D.-C., Li, E.-M., 2021. Integrated single-cell transcriptome analysis reveals heterogeneity of esophageal squamous cell carcinoma microenvironment. Nature Commun. 12 (1), 1–15. http://dx.doi.org/10.1038/s41467-021-27599-5.

Ejima, K., Kim, K.S., Ludema, C., Bento, A.I., Iwanami, S., Fujita, Y., Ohashi, H., Koizumi, Y., Watashi, K., Aihara, K., Nishiura, H., Iwami, S., 2021. Estimation of the incubation period of COVID-19 using viral load data. Epidemics 35, 100454. http://dx.doi.org/10.1016/j.epidem.2021.100454.

Fajnzylber, J., Regan, J., Coxen, K., Corry, H., Wong, C., Rosenthal, A., Worrall, D., Giguel, F., Piechocka-Trocha, A., Atyeo, C., Fischinger, S., Chan, A., Flaherty, K.T., Hall, K., Dougan, M., Ryan, E.T., Gillespie, E., Chishti, R., Li, Y., Jilg, N., Hanidziar, D., Baron, R.M., Baden, L., Tsibris, A.M., Armstrong, K.A., Kuritzkes, D.R., Alter, G., Walker, B.D., Yu, X., Li, J.Z., Abayneh, B.A., Allen, P., Antille, D., Balazs, A., Bals, J., Barbash, M., Bartsch, Y., Boucau, J., Boyce, S., Braley, J., Branch, K., Broderick, K., Carney, J., Chevalier, J., Choudhary, M.C., Chowdhury, N., Cordwell, T., Daley, G., Davidson, S., Desjardins, M., Donahue, L., Drew, D., Einkauf, K., Elizabeth, S., Elliman, A., Etemad, B., Fallon, J., Fedirko, L., Finn, K., Flannery, J., Forde, P., Garcia-Broncano, P., Gettings, E., Golan, D., Goodman, K., Griffin, A., Grimmel, S., Grinke, K., Hartana, C.A., Healy, M., Heller, H., Henault, D., Holland, G., Jiang, C., Jordan, H., Kaplonek, P., Karlson, E.W., Karpell, M., Kayitesi, C., Lam, E.C., LaValle, V., Lefteri, K., Lian, X., Lichterfeld, M., Lingwood, D., Liu, H., Liu, J., Lopez, K., Lu, Y., Luthern, S., Ly, N.L., MacGowan, M., Magispoc, K., Marchewka, J., Martino, B., McNamara, R., Michell, A., Millstrom, I., Miranda, N., Nambu, C., Nelson, S., Noone, M., Novack, L., O'Callaghan, C., Ommerborn, C., Osborn, M., Pacheco, L.C., Phan, N., Pillai, S., Porto, F.A., Rassadkina, Y., Reissis, A., Ruzicka, F., Seiger, K., Selleck, K., Sessa, L., Sharpe, A., Sharr, C., Shin, S., Singh, N., Slaughenhaupt, S., Sheppard, K.S., Sun, W., Sun, X., Suschana, E.L., Talabi, O., Ticheli, H., Weiss, S.T., Wilson, V., Zhu, A., 2020. SARS-CoV-2 viral load is associated with increased disease severity and mortality. Nature Commun. 11 (1), 1–9. http://dx.doi.org/10.1038/s41467-020-19057-5.

Farhang-sardroodi, S., Korosec, C.S., Gholami, S., Craig, M., Moyles, I.R., Ghaemi, M.S., Ooi, H.K., Heffernan, J.M., 2021. Analysis of Host Immunological Response of Adenovirus-Based COVID-19 Vaccines. Vaccines 9 (8), 861.

Gholami, S., Korosec, C.S., Farhang-Sardroodi, S., Dick, D.W., Craig, M., Ghaemi, M.S., Ooi, H.K., Heffernan, J.M., 2023. A mathematical model of protein subunits COVID-19 vaccines. Math. Biosci. 108970. http://dx.doi.org/10.1016/J.MBS.2023.108970.

GomeroBoloye, 2021. Latin Hypercube Sampling and Partial Rank Correlation Coefficient Analysis Applied to an Optimal Control Problem (Ph.D. thesis). University of Tennessee, URL https://trace.tennessee.edu/utk{_}gradthes/1278.

Gonçalves, A., Bertrand, J., Ke, R., Comets, E., de Lamballerie, X., Malvy, D., Pizzorno, A., Terrier, O., Rosa Calatrava, M., Mentré, F., Smith, P., Perelson, A.S., Guedj, J., 2020. Timing of Antiviral Treatment Initiation is Critical to Reduce SARS-CoV-2 Viral Load. CPT: Pharmacomet. Syst. Pharmacol. 9 (9), 509–514. http://dx.doi.org/10.1002/psp4.12543.

Gonçalves, A., Maisonnasse, P., Donati, F., Albert, M., Behillil, S., Contreras, V., Naninck, T., Marlin, R., Solas, C., Pizzorno, A., Lemaitre, J., Kahlaoui, N., Terrier, O., Fang, R.H.T., Enouf, V., Dereuddre-Bosquet, N., Brisebarre, A., Touret, F., Chapon, C., Hoen, B., Lina, B., Calatrava, M.R., de Lamballerie, X., Mentré, F., Le Grand, R., van der Werf, S., Guedj, J., 2021. SARS-CoV-2 viral dynamics in non-human primates. PLoS Comput. Biol. 17 (3), e1008785. http://dx.doi.org/10.1371/JOURNAL.PCBI.1008785.

Goyal, A., Cardozo-Ojeda, E.F., Schiffer, J.T., 2020. Potency and timing of antiviral therapy as determinants of duration of SARS-CoV-2 shedding and intensity of inflammatory response. Sci. Adv. 6 (47), eabc7112. http://dx.doi.org/10.1126/sciadv.abc7112.

Goyal, A., Reeves, D.B., Fabian Cardozo-Ojeda, E., Schiffer, J.T., Mayer, B.T., 2021. Viral load and contact heterogeneity predict sars-cov-2 transmission and super-spreading events. ELife 10, e63537. http://dx.doi.org/10.7554/eLife.63537.

Heffernan, J.M., Smith, R.J., Wahl, L.M., 2005. Perspectives on the basic reproductive ratio. J. R. Soc. Interface 2 (4), 281–293. http://dx.doi.org/10.1098/rsif.2005.0042.

Holder, B.P., Beauchemin, C.A., 2011. Exploring the effect of biological delays in kinetic models of influenza within a host or cell culture. BMC Public Health 11 (1), 1–15. http://dx.doi.org/10.1186/1471-2458-11-S1-S10.

Huang, Y., Chen, S., Yang, Z., Guan, W., Liu, D., Lin, Z., Zhang, Y., Xu, Z., Liu, X., Li, Y., 2020. SARS-CoV-2 viral load in clinical samples from critically ill patients. Am. J. Respir. Crit. Care Med. 201 (11), 1435–1438. http://dx.doi.org/10.1164/rccm.202003-0572LE.

Hurtado, P.J., Kirosingh, A.S., 2019. Generalizations of the 'Linear Chain Trick': incorporating more flexible dwell time distributions into mean field ODE models. J. Math. Biol. 79 (5), 1831–1883. http://dx.doi.org/10.1007/s00285-019-01412-w, arXiv:1808.07571.

Jones, T.C., Biele, G., Mühlemann, B., Veith, T., Schneider, J., Beheim-Schwarzbach, J., Bleicker, T., Tesch, J., Schmidt, M.L., Sander, L.E., Kurth, F., Menzel, P., Schwarzer, R., Zuchowski, M., Hofmann, J., Krumbholz, A., Stein, A., Edelmann, A., Corman, V.M., Drosten, C., 2021. Estimating infectiousness throughout SARS-CoV-2 infection course. Science 373 (6551), eabi5273. http://dx.doi.org/10.1126/science.abi5273.

Kakizoe, Y., Nakaoka, S., Beauchemin, C.A., Morita, S., Mori, H., Igarashi, T., Aihara, K., Miura, T., Iwami, S., 2015. A method to determine the duration of the eclipse phase for in vitro infection with a highly pathogenic SHIV strain. Sci. Rep. 5 (1), 1–14. http://dx.doi.org/10.1038/srep10371.

Ke, R., Martinez, P.P., Smith, R.L., Gibson, L.L., Mirza, A., Conte, M., Gallagher, N., Luo, C.H., Jarrett, J., Zhou, R., Conte, A., Liu, T., Farjo, M., Walden, K.K., Rendon, G., Fields, C.J., Wang, L., Fredrickson, R., Edmonson, D.C., Baughman, M.E., Chiu, K.K., Choi, H., Scardina, K.R., Bradley, S., Gloss, S.L., Reinhart, C., Yedetore, J., Quicksall, J., Owens, A.N., Broach, J., Barton, B., Lazar, P.,

Heetderks, W.J., Robinson, M.L., Mostafa, H.H., Manabe, Y.C., Pekosz, A., McManus, D.D., Brooke, C.B., 2022. Daily longitudinal sampling of SARS-CoV-2 infection reveals substantial heterogeneity in infectiousness. Nat. Microbiol. 7, 640–652. http://dx.doi.org/10.1038/s41564-022-01105-z.

Kim, J.Y., Ko, J.H., Kim, Y., Kim, Y.J., Kim, J.M., Chung, Y.S., Kim, H.M., Han, M.G., Kim, S.Y., Chin, B.S., 2020. Viral load kinetics of SARS-CoV-2 infection in first two patients in Korea. J. Korean Med. Sci. 35 (7), 1–7. http://dx.doi.org/10.3346/jkms.2020.35.e86.

Korosec, C.S., Farhang-Sardroodi, S., Dick, D.W., Gholami, S., Ghaemi, M.S., Moyles, I.R., Craig, M., Ooi, H.K., Heffernan, J.M., 2022. Long-term durability of immune responses to the BNT162b2 and mRNA-1273 vaccines based on dosage, age and sex. Sci. Rep. 12 (1), 21232. http://dx.doi.org/10.1038/s41598-022-25134-0, arXiv:/doi.org/10.1101/2021.10.13.21264957.

Lauer, S.A., Grantz, K.H., Bi, Q., Jones, F.K., Zheng, Q., Meredith, H.R., Azman, A.S., Reich, N.G., Lessler, J., 2020. The Incubation Period of Coronavirus Disease 2019 (COVID-19) From Publicly Reported Confirmed Cases: Estimation and Application. Ann. Intern. Med. 172 (9), 577–582. http://dx.doi.org/10.7326/M20-0504.

Lescure, F.X., Bouadma, L., Nguyen, D., Parisey, M., Wicky, P.H., Behillil, S., Gaymard, A., Bouscambert-Duchamp, M., Donati, F., Le Hingrat, Q., Enouf, V., Houhou-Fidouh, N., Valette, M., Mailles, A., Lucet, J.C., Mentre, F., Duval, X., Descamps, D., Malvy, D., Timsit, J.F., Lina, B., Van-der Werf, S., Yazdanpanah, Y., 2020. Clinical and virological data of the first cases of COVID-19 in Europe: a case series. Lancet Infect. Dis. 20 (6), 697–706. http://dx.doi.org/10.1016/S1473-3099(20)30200-0.

Liew, D.F., Robinson, P.C., 2022. What does endemic COVID-19 mean for the future of rituximab? Lancet Rheumatol. 4 (1), e3–e5.

Lin, J., Law, R., Korosec, C.S., Zhou, C., Koh, H., Ghaemi, S., Samaan, P., Kiang Ooi, H., Matveev, V., Yue, F., Gingras, A.-C., Estacio, A., Buchholz, M., Cheatley, P.L., Mohammadi, A., Kaul, R., Pavinski, K., Mubareka, S., McGeer, A.J., Leis, J.A., Heffernan, J.M., Ostrowski, M., 2022. Longitudinal Assessment of SARS-CoV-2-Specific T Cell Cytokine-Producing Responses for 1 Year Reveals Persistence of Multicytokine Proliferative Responses, with Greater Immunity Associated with Disease Severity. J. Virol. 96 (13), e00509–e00522. http://dx.doi.org/10.1128/jvi.00509-22.

Marc, A., Kerioui, M., Blanquart, F., Bertrand, J., Mitjà, O., Corbacho-Monné, M., Marks, M., Guedj, J., 2021. Quantifying the relationship between sars-cov-2 viral load and infectiousness. eLife 10, 1–15. http://dx.doi.org/10.7554/eLife.69302.

Maziane, M., Lotfi, E.M., Hattaf, K., Yousfi, N., 2015. Dynamics of a Class of HIV Infection Models with Cure of Infected Cells in Eclipse Stage. Acta Biotheor. 63 (4), 363–380. http://dx.doi.org/10.1007/s10441-015-9263-y.

McKay, M.D., Beckman, R.J., Conover, W.J., 2000. A comparison of three methods for selecting values of input variables in the analysis of output from a computer code. Technometrics 42 (1), 55–61. http://dx.doi.org/10.1080/00401706.2000.10485979.

2020. Monolix 2020R1. Lixoft SAS, , a Simulations Plus company, Antony, France.

Moyles, I.R., Heffernan, J.M., Kong, J.D., 2021. Cost and social distancing dynamics in a mathematical model of COVID-19 with application to Ontario, Canada. R. Soc. Open Sci. 8 (2), http://dx.doi.org/10.1098/rsos.201770.

Moyles, I.R., Korosec, C.S., Heffernan, J.M., 2022. Determination of significant immunological timescales from mRNA-LNP-based vaccines in humans. MedRxiv 2022.07.25, http://dx.doi.org/10.1101/2022.07.25.22278031, arXiv:2022.07.25.22278031.

Néant, N., Lingas, G., Le Hingrat, Q., Ghosn, J., Engelmann, I., Lepiller, Q., Gaymard, A., Ferré, V., Hartard, C., Plantier, J.-C., Thibault, V., Marlet, J., Montes, B., Bouiller, K., Lescure, F.-X., Timsit, J.-F., Faure, E., Poissy, J., Chidiac, C., Raffi, F., Kimmoun, A., Etienne, M., Richard, J.-C., Tattevin bb, P., Garot cc, D., Le Moing dd, V., Bachelet ee, D., Tardivon ee, C., Duval, X., Yazdanpanah, Y., Mentré, F., Laouénan, C., Visseaux, B., Guedj, J., 2021. Modeling SARS-CoV-2 viral kinetics and association with mortality in hospitalized patients from the French COVID cohort. Proc. Natl. Acad. Sci. USA 118 (8), e2017962118. http://dx.doi.org/10.1073/pnas.2017962118/-/DCSupplemental.

Pan, Y., Zhang, D., Yang, P., Poon, L.L., Wang, Q., 2020. Viral load of SARS-CoV-2 in clinical samples. Lancet Infect. Dis. 20 (4), 411–412. http://dx.doi.org/10.1016/S1473-3099(20)30113-4.

Pawelek, K.A., Huynh, G.T., Quinlivan, M., Cullinane, A., Rong, L., Perelson, A.S., 2012. Modeling within-host dynamics of influenza virus infection including immune responses. PLoS Comput. Biol. 8 (6), http://dx.doi.org/10.1371/journal.pcbi.1002588.

Perelson, A.S., Ke, R., 2021. Mechanistic Modeling of SARS-CoV-2 and Other Infectious Diseases and the Effects of Therapeutics. Clin. Pharmacol. Therap. 109 (4), 829–840. http://dx.doi.org/10.1002/cpt.2160.

Pinilla, L.T., Holder, B.P., Abed, Y., Boivin, G., Beauchemin, C.A.A., 2012. The H275Y neuraminidase mutation of the pandemic A/H1N1 influenza virus lengthens the eclipse phase and reduces viral output of infected cells, potentially compromising fitness in ferrets. J. Virol. 86 (19), 10651–10660.

Pokhrel, S., Chhetri, R., 2021. A literature review on impact of COVID-19 pandemic on teaching and learning. High. Educ. Future 8 (1), 133–141.

Pujadas, E., Chaudhry, F., McBride, R., Richter, F., Zhao, S., Wajnberg, A., Nadkarni, G., Glicksberg, B.S., Houldsworth, J., Cordon-Cardo, C., 2020. SARS-CoV-2 viral load predicts COVID-19 mortality. Lancet Respir. Med. 8 (9), e70. http://dx.doi.org/10.1016/S2213-2600(20)30354-4.

Ra, S.H., Lim, J.S., Kim, G.-u., Kim, M.J., Jung, J., Kim, S.-H., 2021. Upper respiratory viral load in asymptomatic individuals and mildly symptomatic patients with SARS-CoV-2 infection. Thorax 76 (1), 61–63. http://dx.doi.org/10.1136/thoraxjnl-2020-215042.

Ramratnam, B., Bonhoeffer, S., Binley, J., Hurley, A., Zhang, L., Mittler, J.E., Markowitz, M., Moore, J.P., Perelson, A.S., Ho, D.D., 1999. Rapid production and clearance of HIV-1 and hepatitis C virus assessed by large volume plasma apheresis. Lancet 354 (9192), 1782–1785. http://dx.doi.org/10.1016/S0140-6736(99)02035-8.

Rohatgi, A., 2021. Webplotdigitizer: Version 4.5. URL https://automeris.io/WebPlotDigitizer.

Rong, L., Gilchrist, M.A., Feng, Z., Perelson, A.S., 2007. Modeling within-host HIV-1 dynamics and the evolution of drug resistance: trade-offs between viral enzyme function and drug susceptibility. J. Theoret. Biol. 247 (4), 804–818.

Sandoni, A., Schaffrath Rosario, A., Michel, J., Kuttig, T., Wurm, J., Damerow, S., Iwanowski, H., Finkel, B., Schrick, L., Buchholz, U., Haas, W., Varnaccia, G., Kubisch, U., Jordan, S., Schienkiewitz, A., Nitsche, A., Loss, J., 2022. SARS-CoV-2 viral clearance and viral load kinetics in young children (1–6 years) compared to adults: Results of a longitudinal study in Germany. Front. Pediatr. 10 (November), 1–11. http://dx.doi.org/10.3389/fped.2022.989456.

Sher, A., Niederer, S.A., Mirams, G.R., Kirpichnikova, A., Allen, R., Pathmanathan, P., Gavaghan, D.J., van der Graaf, P.H., Noble, D., 2022. A Quantitative Systems Pharmacology Perspective on the Importance of Parameter Identifiability. Bull. Math. Biol. 84 (3), 1–15. http://dx.doi.org/10.1007/s11538-021-00982-5.

Sigal, D., Reid, J.N., Wahl, L.M., 2018. Effects of transmission bottlenecks on the diversity of influenza a virus. Genetics 210 (3), 1075–1088. http://dx.doi.org/10.1534/genetics.118.301510.

Simon, P.F., De La Vega, M.A., Paradis, É., Mendoza, E., Coombs, K.M., Kobasa, D., Beauchemin, C.A., 2016. Avian influenza viruses that cause highly virulent infections in humans exhibit distinct replicative properties in contrast to human H1N1 viruses. Sci. Rep. 6 (1), 1–13. http://dx.doi.org/10.1038/srep24154.

Singanayagam, A., Hakki, S., Dunning, J., Madon, K.J., Crone, M.A., Koycheva, A., Derqui-Fernandez, N., Barnett, J.L., Whitfield, M.G., Varro, R., Charlett, A., Kundu, R., Fenn, J., Cutajar, J., Quinn, V., Conibear, E., Barclay, W., Freemont, P.S., Taylor, G.P., Ahmad, S., Zambon, M., Ferguson, N.M., Lalvani, A., Badhan, A., Dustan, S., Tejpal, C., Ketkar, A.V., Narean, J.S., Hammett, S., McDermott, E., Pillay, T., Houston, H., Luca, C., Samuel, J., Bremang, S., Evetts, S., Poh, J., Anderson, C., Jackson, D., Miah, S., Ellis, J., Lackenby, A., 2022. Community transmission and viral load kinetics of the SARS-CoV-2 delta (B.1.617.2) variant in vaccinated and unvaccinated individuals in the UK: a prospective, longitudinal, cohort study. Lancet Infect. Dis. 22 (2), 183–195. http://dx.doi.org/10.1016/S1473-3099(21)00648-4.

Stankiewicz Karita, H.C., Dong, T.Q., Johnston, C., Neuzil, K.M., Paasche-Orlow, M.K., Kissinger, P.J., Bershteyn, A., Thorpe, L.E., Deming, M., Kottkamp, A., Laufer, M., Landovitz, R.J., Luk, A., Hoffman, R., Roychoudhury, P., Magaret, C.A., Greninger, A.L., Huang, M.L., Jerome, K.R., Wener, M., Celum, C., Chu, H.Y., Baeten, J.M., Wald, A., Barnabas, R.V., Brown, E.R., 2021. Trajectory of Viral RNA Load among Persons with Incident SARS-CoV-2 G614 Infection (Wuhan Strain) in Association with COVID-19 Symptom Onset and Severity. JAMA Netw. Open 5 (1), 1–12. http://dx.doi.org/10.1001/jamanetworkopen.2021.42796.

Tsukagoshi, H., Shinoda, D., Saito, M., Okayama, K., Sada, M., Kimura, H., Saruki, N., 2021. Relationships between viral load and the clinical course of covid-19. Viruses 13 (2), 2–7. http://dx.doi.org/10.3390/v13020304.

Vafadar, S., Shahdoust, M., Kalirad, A., Zakeri, P., Sadeghi, M., 2021. Competitive exclusion during co-infection as a strategy to prevent the spread of a virus: A computational perspective. PLoS One 16 (2), e0247200. http://dx.doi.org/10.1371/journal.pone.0247200.

Wang, S., Pan, Y., Wang, Q., Miao, H., Brown, A.N., Rong, L., 2020. Modeling the viral dynamics of SARS-CoV-2 infection. Math. Biosci. 328, 108438. http://dx.doi.org/10.1016/j.mbs.2020.108438.

Westblade, L.F., Brar, G., Pinheiro, L.C., Paidoussis, D., Rajan, M., Martin, P., Goyal, P., Sepulveda, J.L., Zhang, L., George, G., Liu, D., Whittier, S., Plate, M., Small, C.B., Rand, J.H., Cushing, M.M., Walsh, T.J., Cooke, J., Safford, M.M., Loda, M., Satlin, M.J., 2020. SARS-CoV-2 Viral Load Predicts Mortality in Patients with and without Cancer Who Are Hospitalized with COVID-19. Cancer Cell 38 (5), 661–671. http://dx.doi.org/10.1016/j.ccell.2020.09.007.

Wölfel, R., Corman, V.M., Guggemos, W., Seilmaier, M., Zange, S., Müller, M.A., Niemeyer, D., Jones, T.C., Vollmar, P., Rothe, C., Hoelscher, M., Bleicker, T., Brünink, S., Schneider, J., Ehmann, R., Zwirglmaier, K., Drosten, C., Wendtner, C., 2020. Virological assessment of hospitalized patients with COVID-2019. Nature 581 (7809), 465–469. http://dx.doi.org/10.1038/s41586-020-2196-x.

Xiong, J., Lipsitz, O., Nasri, F., Lui, L.M., Gill, H., Phan, L., Chen-Li, D., Iacobucci, M., Ho, R., Majeed, A., et al., 2020. Impact of COVID-19 pandemic on mental health in the general population: A systematic review. J. Affect. Disord. 277, 55–64.

Young, B.E., Ong, S.W.X., Kalimuddin, S., Low, J.G., Tan, S.Y., Loh, J., Ng, O.T., Marimuthu, K., Ang, L.W., Mak, T.M., Lau, S.K., Anderson, D.E., Chan, K.S., Tan, T.Y., Ng, T.Y., Cui, L., Said, Z., Kurupatham, L., Chen, M.I., Chan, M., Vasoo, S., Wang, L.F., Tan, B.H., Lin, R.T.P., Lee, V.J.M., Leo, Y.S., Lye, D.C., 2020. Epidemiologic Features and Clinical Course of Patients Infected with SARS-CoV-2 in Singapore. JAMA 323 (15), 1488–1494. http://dx.doi.org/10.1001/jama.2020.3204.